

A high-level programming-language implementation of topology optimization applied to steady-state Navier–Stokes flow

Laurits Højgaard Olesen, Fridolin Okkels, and Henrik Bruus

MIC – Department of Micro and Nanotechnology,

Technical University of Denmark, DK-2800 Kongens Lyngby, Denmark

(Dated: 11 October 2004)

We present a versatile high-level programming-language implementation of nonlinear topology optimization. Our implementation is based on the commercial software package FEMLAB. For problems that can be formulated in the simple divergence form it allows a wide range of optimization objectives to be dealt with easily. We exemplify our method by studies of steady-state Navier–Stokes flow problems, thus extending the work by Borrvall and Petersson on topology optimization of fluids in Stokes flow [Int. J. Num. Meth. Fluids 41, 77 (2003)]. We analyze the physical aspects of the solutions and how they are affected by different parameters of the optimization algorithm. A complete example of our implementation is included as FEMLAB code in an appendix.

Keywords: topology optimization, Navier–Stokes flow, inertial effects, Femlab

I. INTRODUCTION

The material distribution method in topology optimization was originally developed for stiffness design of mechanical structures [2] but has now been extended to a multitude of design problems in structural mechanics as well as to optics and acoustics [3, 4, 5, 6]. Recently Borrvall and Petersson introduced the method for fluids in Stokes flow [1]. However, it is desirable to extend the method to fluids described in a full Navier–Stokes flow; a direction pioneered by the work of Sigmund and Gersborg-Hansen [7, 8].

In the present work we present such an extension by introducing a versatile high-level programming-language implementation of nonlinear topology optimization. Our implementation is based on the commercial software package FEMLAB. It has a wider range of applicability than the Navier–Stokes problems studied here, since any problem that can be formulated in the simple divergence form can be treated. Moreover it allows a wide range of optimization objectives to be dealt with easily.

Extending the topology optimization method to new physical domains generally involves some rethinking of the design problem and some ‘trial and error’ to determine suitable design objectives. It also requires the analysis and implementation of the problem problem in the finite element method (FEM). This process is accelerated a lot by using a high-level FEM library or package that allows different physical models to be joined and eases the tasks of, e.g., geometry setup, mesh generation and postprocessing. The disadvantage is that high-level packages tend to have rather complex data structure, not easily accessible to the user. This can complicate the actual implementation of the problem because the sensitivity analysis is traditionally formulated in a low-level manner.

In this work we have used the commercial finite-element package FEMLAB both for the solution of the flow problem and for the sensitivity analysis required by the optimization algorithm. We show how this sensitivity analysis can be performed in FEMLAB in a simple way that is almost independent of the particular physical problem studied. This approach may prove even more useful for multiphysical extensions, where the flow problem is coupled to, e.g., with heat conduction, convection-diffusion of solutes, and deformation of elastic channel walls in valves and flow rectifiers.

The paper is organized as follows: In Sec. II we introduce the topology optimization method for fluids in Navier–Stokes flow, and discuss the objective of designing fluidic devices or channel networks for which the power dissipation is minimized. In Sec. III we express the Navier–Stokes equations in a generic divergence form that allows them to be solved with FEMLAB. This form encompasses a wide range of physical problems. We also work out the sensitivity analysis for a general class of integral-type optimization objectives in such a way that the built-in symbolic differentiation tools of FEMLAB can be exploited. In Sec. IV we present our two numerical examples that illustrates different aspects and problems to consider: The first example deals with designing a structure that can guide the flow in the reverse direction of the applied pressure drop. The general outcome of the optimization is an *S*-shaped channel, but the example illustrates how the detailed structure depends on the choice of the parameters of the algorithm. The second example deals with a four terminal device for which the fluidic channel design that minimizes the power dissipation shows a Reynolds number dependence. As the Reynolds number is increased a transition occurs between two topologically different solutions, and we discuss how the position of the transition depends on the choice of initial conditions. Finally in the appendix we include a transcript of our FEMLAB code required for solving the second numerical example. The code amounts to 111 lines excluding the optimization algorithm, that can be obtained by contacting K. Svanberg [9, 10].

II. TOPOLOGY OPTIMIZATION FOR NAVIER–STOKES FLOW IN STEADY STATE

Although our high-level programming-language implementation is generally applicable we have chosen to start on the concrete level by treating the basic equations for our main example: the full steady-state Navier–Stokes flow problem for incompressible fluids.

We consider a given computational domain Ω with appropriate boundary conditions for the flow given on the domain boundary $\partial\Omega$. The goal of the optimization is to distribute a certain amount of solid material inside Ω such that the material layout defines a fluidic device or channel network that is optimal with respect to some objective, formulated as a function of the variables, e.g., minimization the power dissipated inside the domain.

The basic principle in the material distribution method for topology optimization is to replace the original discrete design problem with a continuous one where the material density is allowed to vary continuously between solid and void. Thus in our flow problem we assume the design domain to be filled with some idealized porous material of spatially varying permeability. Solid wall and open channels then correspond to the limits of very low and very high permeability, respectively.

In the final design there should preferably be no regions at intermediate permeability since otherwise it cannot be interpreted as a solution to the original discret problem. Alternatively it may be possible to fabricate the device from polymeric materials that naturally have a finite permeability to the fluid.

A. Governing equations for flow in idealized porous media

We assume that the fluid flowing in the idealized porous medium is subject to a friction force \mathbf{f} which is proportional to the fluid velocity \mathbf{v} , c.f. Darcy's law. Thus $\mathbf{f} = -\alpha\mathbf{v}$, where $\alpha(\mathbf{r})$ is the inverse of the local permeability of the medium at position \mathbf{r} . These properties of the idealized porous medium may only be approximately valid for an actual medium. However, the assumptions are not in conflict with any fundamental physical law, and since the converged solutions contain only solid walls and open channels, the specific nature of the idealized porous medium is of no consequence.

The flow problem is described in terms of the fluid velocity field $\mathbf{v}(\mathbf{r})$ and pressure $p(\mathbf{r})$. The governing equations are the steady state Navier–Stokes equation and the incompressibility constraint

$$\rho(\mathbf{v} \cdot \nabla)\mathbf{v} = \nabla \cdot \boldsymbol{\sigma} - \alpha\mathbf{v}, \quad (1)$$

$$\nabla \cdot \mathbf{v} = 0, \quad (2)$$

where ρ is the mass density of the fluid. For an incompressible Newtonian fluid the components σ_{ij} of the Cauchy stress tensor $\boldsymbol{\sigma}$ are given by

$$\sigma_{ij} = -p\delta_{ij} + \eta\left(\frac{\partial v_i}{\partial x_j} + \frac{\partial v_j}{\partial x_i}\right), \quad (3)$$

where η is the dynamic viscosity. The formalism is valid in three dimensions, but for simplicity we shall consider only two-dimensional problems, i.e., we assume translational invariance in the third dimension and set $\mathbf{r} = (x_1, x_2)$ and $\mathbf{v} = (v_1(\mathbf{r}), v_2(\mathbf{r}))$. The boundary conditions will typically be either Dirichlet type specifying the velocity field \mathbf{v} on the boundary or Neumann type specifying the external forces $\mathbf{n} \cdot \boldsymbol{\sigma}$.

It is convenient to introduce a design variable field $\gamma(\mathbf{r})$ controlling the local permeability of the medium. We let γ vary between zero and unity, with $\gamma = 0$ corresponding to solid material and $\gamma = 1$ to no material. Following Ref. [1] we then relate the local inverse permeability $\alpha(\mathbf{r})$ to the design field $\gamma(\mathbf{r})$ by the convex interpolation

$$\alpha(\gamma) \equiv \alpha_{\min} + (\alpha_{\max} - \alpha_{\min}) \frac{q[1 - \gamma]}{q + \gamma}, \quad (4)$$

where q is a real and positive parameter used to tune the shape of $\alpha(\gamma)$. Ideally, impermeable solid walls would be obtained with $\alpha_{\max} = \infty$, but for numerical reasons we need to choose a finite value for α_{\max} . For the minimal value we choose $\alpha_{\min} = 0$. [14]

For a given material distribution $\gamma(\mathbf{r})$ there are two dimensionless numbers characterizing the flow, namely the Reynolds number

$$Re = \frac{\rho \ell v}{\eta} \quad (5)$$

describing the ratio between inertia and viscous forces, and the Darcy number

$$Da = \frac{\eta}{\alpha_{\max} \ell^2} \quad (6)$$

describing the ratio between viscous and porous friction forces. Here ℓ is a characteristic length scale of the system and v a characteristic velocity.

Almost impermeable solid material is obtained for very low Darcy numbers, in practice $Da \lesssim 10^{-3}$. Further insight into the meaning of the Darcy number is gained by considering Poiseuille flow in a channel or slit of width ℓ between two infinite parallel plates of porous material. In this case the fluid velocity inside the porous walls decays on a length scale $\sqrt{Da} \ell = \sqrt{\eta/\alpha_{\max}}$.

B. Power dissipation

In the pioneering work by Borrvall and Petersson [1] the main focus was on minimizing the power dissipation in the fluid. The total power Φ dissipated inside the fluidic system (per unit length in the third dimension) is given by [11]

$$\Phi(\mathbf{v}, p, \gamma) = \int_{\Omega} \left[\frac{1}{2} \eta \sum_{i,j} \left(\frac{\partial v_i}{\partial x_j} + \frac{\partial v_j}{\partial x_i} \right)^2 + \sum_i \alpha(\gamma) v_i^2 \right] \mathrm{d}\mathbf{r}. \quad (7a)$$

In steady-state this is equal to the sum of the work done on the system by the external forces and the kinetic energy convected into it,

$$\Phi(\mathbf{v}, p, \gamma) = \int_{\partial\Omega} \sum_{i,j} \left[n_i \sigma_{ij} v_j - n_i v_i \left(\frac{1}{2} \rho v_j^2 \right) \right] \mathrm{d}s. \quad (7b)$$

Here \mathbf{n} is a unit outward normal vector such that $\mathbf{n} \cdot \boldsymbol{\sigma}$ is the external force acting on the system boundary and $\mathbf{n} \cdot \boldsymbol{\sigma} \cdot \mathbf{v}$ is the work done on the system by this force. Moreover, in the common case where the geometry and boundary conditions are such that the no-slip condition $\mathbf{v} = \mathbf{0}$ applies on all external solid walls, while on the inlet and outlet boundaries \mathbf{v} is parallel to \mathbf{n} and $(\mathbf{n} \cdot \nabla) \mathbf{v} = 0$, [15] Eq. (7b) reduces to

$$\Phi(\mathbf{v}, p, \gamma) = \int_{\partial\Omega} -\mathbf{n} \cdot \mathbf{v} (p + \frac{1}{2} \rho v^2) \mathrm{d}s. \quad (7c)$$

Borrvall and Petersson showed that for Stokes flow with Dirichlet boundary conditions everywhere on the boundary $\partial\Omega$, the problem of minimizing the total power dissipation inside the fluidic device subject to a volume constraint on the material distribution is mathematically well-posed. Moreover it was proven that in the case where $\alpha(\gamma)$ is a linear function, the optimal material distribution is fully discrete-valued.

When $\alpha(\gamma)$ is not linear but *convex* then the solid/void interfaces in the optimal solution are not discrete zero/unity transitions but slightly smeared out. Convexity implies that the (negative value of the) slope of α at $\gamma = 0$ is larger than at $\gamma = 1$; therefore there will be a neighbourhood around the discrete interface where it pays to move material from the solid side to the void. Using the interpolation in Eq. (4) we have $\alpha'(0) = (\alpha_{\min} - \alpha_{\max}) \frac{1+q}{q}$ whereas $\alpha'(1) = (\alpha_{\min} - \alpha_{\max}) \frac{q}{1+q}$. For large values of q the interpolation is almost linear and we expect almost discrete interfaces, whereas for small q we expect smeared out interfaces in the optimized solution.

Consider the case when Eq. (7c) applies. If the system is driven with a prescribed flow rate then minimizing the total power dissipation is clearly equivalent to minimizing the pressure drop across the system. Conversely, if the system is driven at a prescribed pressure drop, then the natural design objective will be to maximize the flow rate which is equivalent to maximizing the dissipated power, c.f. Eq. (7c). In either case the objective can be described as minimizing the hydraulic resistance of the system.

For problems with more complex design objectives, such as a minimax problem for the flow rate through several different outlets, there will typically be no analog in terms of total dissipated power. In such cases there is no guarantee for the existence of a unique optimal solution, and one has to be extra careful when formulating the design problem.

III. GENERALIZED FORMULATION OF THE OPTIMIZATION PROBLEM

For a given material distribution we solve the Navier–Stokes flow problem using the commercial finite element software FEMLAB. FEMLAB provides both a graphical front-end and a library of high-level scripting tools based on

the MATLAB programming language, and it allows the user to solve a wide range of physical problems by simply typing in the strong form of the governing equations as text expressions. The equations must comply with a generic divergence form that eases the conversion to weak form required for the finite element solution. Still, this is the natural way of expressing most physical problems originating from conservation laws.

Since we have chosen fluidics as our main example, we begin by expressing the incompressible Navier–Stokes flow problem in divergence form. Then we state the optimization problem with a general form of the design objective function and perform the discretization and sensitivity analysis based on this generalized formulation. This last step ensures the applicability of our method to most problems that can be formulated in the divergence form.

A. The flow problem in divergence form

We first introduce the velocity-pressure vector $\mathbf{u} = [v_1, v_2, p]$ and define for $i = 1, 2, 3$ the quantities $\mathbf{\Gamma}_i$ and F_i as

$$\mathbf{\Gamma}_1 \equiv \begin{bmatrix} \sigma_{11} \\ \sigma_{21} \end{bmatrix}, \quad \mathbf{\Gamma}_2 \equiv \begin{bmatrix} \sigma_{12} \\ \sigma_{22} \end{bmatrix}, \quad \mathbf{\Gamma}_3 \equiv \begin{bmatrix} 0 \\ 0 \end{bmatrix}, \quad (8)$$

and

$$F_1 \equiv \rho(\mathbf{v} \cdot \nabla)v_1 + \alpha(\gamma)v_1, \quad F_2 \equiv \rho(\mathbf{v} \cdot \nabla)v_2 + \alpha(\gamma)v_2, \quad F_3 \equiv \nabla \cdot \mathbf{v}. \quad (9)$$

Using this, Eqs. (1) and (2) can be written in divergence form as

$$\nabla \cdot \mathbf{\Gamma}_i = F_i \quad \text{in } \Omega, \quad (10a)$$

$$R_i = 0 \quad \text{on } \partial\Omega, \quad (10b)$$

$$-\mathbf{n} \cdot \mathbf{\Gamma}_i = G_i + \sum_{j=1}^3 \frac{\partial R_j}{\partial u_i} \mu_j \quad \text{on } \partial\Omega, \quad (10c)$$

where $\mathbf{\Gamma}_i$ and F_i are understood to be functions of the solution \mathbf{u} , its gradient $\nabla \mathbf{u}$, and of the design variable γ . The quantity $R_i(\mathbf{u}, \gamma)$ in Eq. (10b) describes Dirichlet type boundary conditions. For example, fluid no-slip boundary conditions are obtained by defining $R_1 \equiv v_1$ and $R_2 \equiv v_2$ on the external solid walls. The quantity $G_i(\mathbf{u}, \gamma)$ in Eq. (10c) describe Neumann type boundary conditions, and μ_i denote the Lagrange multiplier necessary to enforce the constraint $R_i = 0$, e.g., the force with which the solid wall has to act upon the fluid to enforce the no-slip boundary condition. Notice, that to enforce Neumann conditions the Lagrange multiplier term in 10c has to be zero. This can be obtained by choosing the zero-function $R_i \equiv 0$ for the Dirichlet constraint. In addition this choice satisfies Eq. (10b) trivially.

B. The objective function

In general the design objective for the optimization is stated as the minimization of a certain *objective function* $\Phi(\mathbf{u}, \gamma)$. We shall consider a generic integral-type objective function of the form

$$\Phi(\mathbf{u}, \gamma) = \int_{\Omega} A(\mathbf{u}, \gamma) \, d\mathbf{r} + \int_{\partial\Omega} B(\mathbf{u}, \gamma) \, ds. \quad (11)$$

In particular, we can treat the design objective of minimizing the power dissipation inside the fluidic domain by taking, c.f. Eq. (7a)

$$A \equiv \frac{1}{2}\eta \sum_{i,j} \left(\frac{\partial v_i}{\partial x_j} + \frac{\partial v_j}{\partial x_i} \right)^2 + \sum_i \alpha(\gamma)v_i^2 \quad \text{in } \Omega \quad \text{and} \quad B \equiv 0 \quad \text{on } \partial\Omega. \quad (12)$$

Alternatively, the objective of maximizing the flow out through a particular boundary segment $\partial\Omega_o$ is obtained by choosing

$$A \equiv 0 \quad \text{in } \Omega \quad \text{and} \quad B \equiv \begin{cases} -\mathbf{n} \cdot \mathbf{v} & \text{on } \partial\Omega_o, \\ 0 & \text{on } \partial\Omega \setminus \partial\Omega_o. \end{cases} \quad (13)$$

And, as a final example, objectives related to N discrete points \mathbf{r}_k can be treated using Dirac delta functions as

$$A \equiv \sum_{k=1}^N A_k \delta(\mathbf{r} - \mathbf{r}_k) \quad \text{in } \Omega \quad \text{and} \quad B \equiv 0 \quad \text{on } \partial\Omega. \quad (14)$$

C. Optimization problem

The optimal design problem can now be stated as a continuous constrained nonlinear optimization problem:

$$\min_{\gamma} \Phi(\mathbf{u}, \gamma) \quad (15a)$$

$$\text{subject to } \frac{1}{|\Omega|} \int_{\Omega} \gamma(\mathbf{r}) d\mathbf{r} - \beta \leq 0, \quad \text{Volume constraint} \quad (15b)$$

$$0 \leq \gamma(\mathbf{r}) \leq 1, \quad \text{Design variable bounds} \quad (15c)$$

$$\nabla \cdot \mathbf{\Gamma}_i = F_i, \quad \text{Governing equations} \quad (15d)$$

$$R_i = 0, \quad \text{Dirichlet b.c.} \quad (15e)$$

$$-\mathbf{n} \cdot \mathbf{\Gamma}_i = G_i + \sum_{j=1}^3 \frac{\partial R_j}{\partial u_i} \mu_j, \quad \text{Neumann b.c.} \quad (15f)$$

With the volume constraint we require that at most a fraction β of the total volume $|\Omega|$ should be void.

The very reason for replacing the original discrete design problem with a continuous one by assuming a porous and permeable material, is that it allows the use of efficient mathematical programming methods for smooth problems. We have chosen the popular method of moving asymptotes (MMA), which is designed for problems with a large number of degrees-of-freedom and thus well-suited for topology optimization [9, 10]. It is a gradient-based algorithm requiring information about the derivative with respect to γ of both the objective function Φ and the constraints. Notice that for any γ the governing equations allow us to solve for \mathbf{u} ; therefore in effect they define $\mathbf{u}[\gamma]$ as an implicit function. The gradient of Φ is then obtained using the chain rule

$$\frac{d}{d\gamma} [\Phi(\mathbf{u}[\gamma], \gamma)] = \frac{\partial \Phi}{\partial \gamma} + \int_{\Omega} \frac{\partial \Phi}{\partial \mathbf{u}} \cdot \frac{\partial \mathbf{u}}{\partial \gamma} d\mathbf{r}. \quad (16)$$

However, because $\mathbf{u}[\gamma]$ is implicit, it is impractical to evaluate the derivative $\partial \mathbf{u} / \partial \gamma$ directly. Instead, we use the adjoint method to eliminate it from Eq. (16) by computing a set of Lagrange multipliers for Eqs. (15d)-(15f) considered as constraints [12]. For details see Sec. III D.

The optimization process is iterative and the k th iteration consists of three steps:

- (i) Given a guess $\gamma^{(k)}$ for the optimal material distribution we first solve Eqs. (15d)-(15f) for $\mathbf{u}^{(k)}$ as a finite element problem using FEMLAB.
- (ii) Next the sensitivity analysis is performed where the gradient of the objective and constraints with respect to γ is evaluated. In order to eliminate $\partial \mathbf{u} / \partial \gamma$ from Eq. (16) we solve the adjoint problem of Eqs. (15d)-(15f) for the Lagrange multipliers $\tilde{\mathbf{u}}^{(k)}$, also using FEMLAB.
- (iii) Finally we use MMA to obtain a new guess $\gamma^{(k+1)}$ for the optimal design based on the gradient information and the past iteration history.

Of those, step (i) is the most expensive computationally since it involves the solution of a nonlinear partial differential equation.

D. Discretization and sensitivity analysis

The starting point of the FEM analysis is to approximate the solution component u_i using a set of finite element basis functions $\{\varphi_{i,n}(\mathbf{r})\}$,

$$u_i(\mathbf{r}) = \sum_n u_{i,n} \varphi_{i,n}(\mathbf{r}), \quad (17)$$

where $u_{i,n}$ are the expansion coefficients. Similiarly, the design variable field $\gamma(\mathbf{r})$ is expressed as

$$\gamma(\mathbf{r}) = \sum_n \gamma_n \varphi_{4,n}(\mathbf{r}). \quad (18)$$

For our incompressible Navier–Stokes problem we use the standard Taylor–Hood element pair with quadratic velocity approximation and linear pressure. For the design variable we have chosen the linear Lagrange element.[16]

The problem Eqs. (10a) to (10c) is discretized by the standard Galerkin method and takes the form

$$\mathbf{L}_i(\mathbf{U}, \boldsymbol{\gamma}) - \sum_{j=1}^3 \mathbf{N}_{ji}^T \boldsymbol{\Lambda}_j = \mathbf{0} \quad \text{and} \quad \mathbf{M}_i(\mathbf{U}, \boldsymbol{\gamma}) = \mathbf{0}, \quad (19)$$

where \mathbf{U}_i , $\boldsymbol{\Lambda}_i$, and $\boldsymbol{\gamma}$ are column vectors holding all the expansion coefficients for the solution $u_{i,n}$, the Lagrange multipliers $\mu_{i,n}$, and the design variable field γ_n , respectively. The column vector \mathbf{L}_i contains the projection of Eq. (10a) onto $\varphi_{i,n}$ which upon partial integration is given by

$$\mathbf{L}_{i,n} = \int_{\Omega} (\varphi_{i,n} F_i + \nabla \varphi_{i,n} \cdot \boldsymbol{\Gamma}_i) \, d\mathbf{r} + \int_{\partial\Omega} \varphi_{i,n} G_i \, ds. \quad (20)$$

The column vector \mathbf{M}_i contains the pointwise enforcement of the Dirichlet constraint Eq. (10b)

$$\mathbf{M}_{i,n} = R_i(\mathbf{u}(\mathbf{r}_{i,n})). \quad (21)$$

Finally, the matrix $\mathbf{N}_{ij} = -\partial \mathbf{M}_i / \partial \mathbf{U}_j$ describes the coupling to the Lagrange multipliers in Eq. (10c). The solution of the nonlinear system in Eq. (19) above corresponds to step (i) in k th iteration. The sensitivity analysis in step (ii) requires us to compute

$$\frac{d}{d\boldsymbol{\gamma}} [\Phi(\mathbf{U}(\boldsymbol{\gamma}), \boldsymbol{\gamma})] = \frac{\partial \Phi}{\partial \boldsymbol{\gamma}} + \sum_{i=1}^3 \frac{\partial \Phi}{\partial \mathbf{U}_i} \frac{\partial \mathbf{U}_i}{\partial \boldsymbol{\gamma}}, \quad (22a)$$

which is done using the standard adjoint method [12]. By construction we have for any $\boldsymbol{\gamma}$ that $\mathbf{L}_i(\mathbf{U}(\boldsymbol{\gamma}), \boldsymbol{\gamma}) - \sum_{j=1}^3 \mathbf{N}_{ji}^T \boldsymbol{\Lambda}_j(\boldsymbol{\gamma}) = \mathbf{0}$ and $\mathbf{M}_i(\mathbf{U}(\boldsymbol{\gamma}), \boldsymbol{\gamma}) = \mathbf{0}$. Therefore also the derivative of those quantities with respect to $\boldsymbol{\gamma}$ is zero, and adding any multiple, say $\tilde{\mathbf{U}}_i$ and $\tilde{\boldsymbol{\Lambda}}_i$, of them to Eq. (22a) does not change the result

$$\begin{aligned} \frac{d}{d\boldsymbol{\gamma}} [\Phi(\mathbf{U}(\boldsymbol{\gamma}), \boldsymbol{\gamma})] &= \frac{\partial \Phi}{\partial \boldsymbol{\gamma}} + \sum_{i=1}^3 \frac{\partial \Phi}{\partial \mathbf{U}_i} \frac{\partial \mathbf{U}_i}{\partial \boldsymbol{\gamma}} + \sum_{i=1}^3 \left[\tilde{\mathbf{U}}_i^T \frac{\partial}{\partial \boldsymbol{\gamma}} \left(\mathbf{L}_i - \sum_{j=1}^3 \mathbf{N}_{ji}^T \boldsymbol{\Lambda}_j \right) + \tilde{\boldsymbol{\Lambda}}_i^T \frac{\partial \mathbf{M}_i}{\partial \boldsymbol{\gamma}} \right] \\ &= \frac{\partial \Phi}{\partial \boldsymbol{\gamma}} + \sum_{i=1}^3 \left(\tilde{\mathbf{U}}_i^T \frac{\partial \mathbf{L}_i}{\partial \boldsymbol{\gamma}} + \tilde{\boldsymbol{\Lambda}}_i^T \frac{\partial \mathbf{M}_i}{\partial \boldsymbol{\gamma}} \right) \\ &\quad + \sum_{i=1}^3 \left[\frac{\partial \Phi}{\partial \mathbf{U}_i} + \sum_{j=1}^3 \left(\tilde{\mathbf{U}}_j^T \frac{\partial \mathbf{L}_i}{\partial \mathbf{U}_j} + \tilde{\boldsymbol{\Lambda}}_j^T \mathbf{N}_{ji} \right) \right] \frac{\partial \mathbf{U}_i}{\partial \boldsymbol{\gamma}} + \sum_{i=1}^3 \left[\sum_{j=1}^3 \tilde{\mathbf{U}}_j^T \mathbf{N}_{ij}^T \right] \frac{\partial \boldsymbol{\Lambda}_i}{\partial \boldsymbol{\gamma}}. \end{aligned} \quad (22b)$$

We see that the derivatives $\partial \mathbf{U}_i / \partial \boldsymbol{\gamma}$ and $\partial \boldsymbol{\Lambda}_i / \partial \boldsymbol{\gamma}$ of the implicit functions can be eliminated by choosing $\tilde{\mathbf{U}}_i$ and $\tilde{\boldsymbol{\Lambda}}_i$ such that

$$\sum_{j=1}^3 \left(\mathbf{K}_{ji}^T \tilde{\mathbf{U}}_j - \mathbf{N}_{ji}^T \tilde{\boldsymbol{\Lambda}}_j \right) = \frac{\partial \Phi}{\partial \mathbf{U}_i} \quad \text{and} \quad \sum_{j=1}^3 \mathbf{N}_{ij} \tilde{\mathbf{U}}_j = \mathbf{0}, \quad (23)$$

where we introduced $\mathbf{K}_{ij} = -\partial \mathbf{L}_i / \partial \mathbf{U}_j$. This problem is the adjoint of Eq. (19) and $\tilde{\mathbf{U}}$ and $\tilde{\boldsymbol{\Lambda}}$ are the corresponding Lagrange multipliers.

E. Implementation aspects

We end this section by discussing a few issues on the implementation of topology optimization using FEMLAB. Firstly there is the question of how to represent the design variable $\gamma(\mathbf{r})$. The governing equations as expressed by $\boldsymbol{\Gamma}_i$ and F_i in Eq. (10a) depend not only on the solution \mathbf{u} but also on γ , and the implementation should allow for this dependence in an efficient way. Here our simple and straightforward approach is to include γ as an extra dependent variable on equal footing with the velocity field and pressure, i.e., we append it to the velocity-pressure vector, redefining \mathbf{u} as

$$\mathbf{u} \equiv [v_1, v_2, p, \gamma]. \quad (24)$$

This was already anticipated when we denoted the basis set for γ by $\{\phi_{4,n}(\mathbf{r})\}$. By making γ available as a field variable we can take full advantage of all the symbolic differentiation, matrix, and postprocessing tools for analysing and displaying the material distribution. Appending γ to the list of dependent variables we are required to define a fourth governing equation. However, since we are never actually going to solve this equation, but rather update γ based on the MMA step, we simply define

$$\boldsymbol{\Gamma}_4 \equiv \begin{bmatrix} 0 \\ 0 \end{bmatrix}, \quad F_4 \equiv 0, \quad G_4 \equiv 0, \quad R_4 \equiv 0. \quad (25)$$

It is crucial then that the finite element solver allows different parts of the problem to be solved in a decoupled manner, i.e., it must be possible to solve Eqs. (10a)-(10c) for u_i for $i = 1, 2, 3$ while keeping u_4 , i.e., γ , fixed.

In FEMLAB the nonlinear problem Eq. (19) is solved using the damped Newton method [13]. Therefore the matrices $\mathbf{K}_{ij} = -\partial \mathbf{L}_i / \partial \mathbf{U}_j$ and $\mathbf{N}_{ij} = -\partial \mathbf{M}_i / \partial \mathbf{U}_j$ appearing in the adjoint problem Eq. (23) are computed automatically as part of the solution process and can be obtained directly as MATLAB sparse matrices. They are given by

$$\begin{aligned} \mathbf{K}_{ij,nm} = & - \int_{\Omega} \left(\varphi_{i,n} \left[\frac{\partial F_i}{\partial u_j} \varphi_{j,m} + \frac{\partial F_i}{\partial \nabla u_j} \cdot \nabla \varphi_{j,m} \right] + \nabla \varphi_{i,n} \cdot \left[\frac{\partial \boldsymbol{\Gamma}_i}{\partial u_j} \varphi_{j,m} + \frac{\partial \boldsymbol{\Gamma}_i}{\partial \nabla u_j} \cdot \nabla \varphi_{j,m} \right] \right) \mathrm{d}\mathbf{r} \\ & - \int_{\partial\Omega} \varphi_{i,n} \frac{\partial G_i}{\partial u_j} \varphi_{j,m} \mathrm{d}s \end{aligned} \quad (26)$$

and

$$\mathbf{N}_{ij,nm} = -\frac{\partial R_i}{\partial u_j} \Big|_{\mathbf{r}_{i,n}} \varphi_{j,m}(\mathbf{r}_{i,n}). \quad (27)$$

Regarding the right-hand side vector $\partial\Phi/\partial\mathbf{U}_i$ in Eq. (23), notice that for a general objective as Eq. (11), it has the form

$$\frac{\partial\Phi}{\partial u_{i,n}} = \int_{\Omega} \left(\frac{\partial A}{\partial u_i} + \frac{\partial A}{\partial \nabla u_i} \cdot \nabla \right) \varphi_{i,n} \mathrm{d}\mathbf{r} + \int_{\partial\Omega} \frac{\partial B}{\partial u_i} \varphi_{i,n} \mathrm{d}s. \quad (28)$$

It is not in the spirit of a high-level finite element package to program the assembly of this vector by hand. In stead we employ the built-in assembly subroutine of FEMLAB. We construct a copy of the original problem sharing the geometry, finite element mesh, and degree-of-freedom numbering with the original. Only we replace the original fields $\boldsymbol{\Gamma}_i$, F_i , and G_i with

$$\tilde{\boldsymbol{\Gamma}}_i = \frac{\partial A}{\partial \nabla u_i}, \quad \tilde{F}_i = \frac{\partial A}{\partial u_i}, \quad \text{and} \quad \tilde{G}_i = \frac{\partial B}{\partial u_i}. \quad (29)$$

Assembling the right-hand-side vector $\tilde{\mathbf{L}}_i$ with this definition yields exactly Eq. (28), c.f. Eq. (20). An extra convenience in FEMLAB is that we can rely on the built-in symbolic differentiation tools to compute the derivatives $\partial A/\partial u_i$ etc. In order to try out a new objective for the optimization problem, the user essentially only needs to change the text expressions defining the quantities A and B .

Finally solving the adjoint problem Eq. (23) for $\tilde{\mathbf{U}}_i$ and $\tilde{\boldsymbol{\Lambda}}_i$ to eliminate $\partial\mathbf{U}_i/\partial\boldsymbol{\gamma}$ and $\partial\boldsymbol{\Lambda}_i/\partial\boldsymbol{\gamma}$ for $i = 1, 2, 3$ in Eq. (22b) we can evaluate the sensitivity

$$\begin{aligned} \frac{d}{d\boldsymbol{\gamma}} [\Phi(\mathbf{U}, \boldsymbol{\gamma})] &= \frac{\partial\Phi}{\partial\boldsymbol{\gamma}} + \sum_{j=1}^3 \left(\frac{\partial \mathbf{L}_j}{\partial\boldsymbol{\gamma}} \right)^T \tilde{\mathbf{U}}_j + \left(\frac{\partial \mathbf{M}_j}{\partial\boldsymbol{\gamma}} \right)^T \tilde{\boldsymbol{\Lambda}}_j \\ &= \tilde{\mathbf{L}}_4 - \sum_{j=1}^3 \left(\mathbf{K}_{j4}^T \tilde{\mathbf{U}}_j + \mathbf{N}_{j4}^T \tilde{\boldsymbol{\Lambda}}_j \right), \end{aligned} \quad (30)$$

where $\mathbf{K}_{i4} = -\partial \mathbf{L}_i / \partial \boldsymbol{\gamma}$, $\mathbf{N}_{i,4} = -\partial \mathbf{M}_i / \partial \boldsymbol{\gamma}$, and $\tilde{\mathbf{L}}_4 = \partial\Phi/\partial\boldsymbol{\gamma}$ in accordance with $\mathbf{U}_4 = \boldsymbol{\gamma}$. Since the fourth variable γ is treated on equal footing with the other three variables, all expressions required to compute the matrices $\mathbf{K}_{i,4}$ and $\mathbf{N}_{i,4}$ come out of the standard linearization of the problem. This is yet another advantage of including γ as an extra dependent variable.

When dealing with a problem with a volume constraint as in Eq. (15b), it is necessary to compute the derivative of the constraint with respect to $\boldsymbol{\gamma}$,

$$\frac{\partial}{\partial\gamma_n} \left[\frac{1}{|\Omega|} \int_{\Omega} \gamma(\mathbf{r}) \mathrm{d}\mathbf{r} - \beta \right] = \frac{1}{|\Omega|} \int_{\Omega} \varphi_{n,4}(\mathbf{r}) \mathrm{d}\mathbf{r}, \quad (31)$$

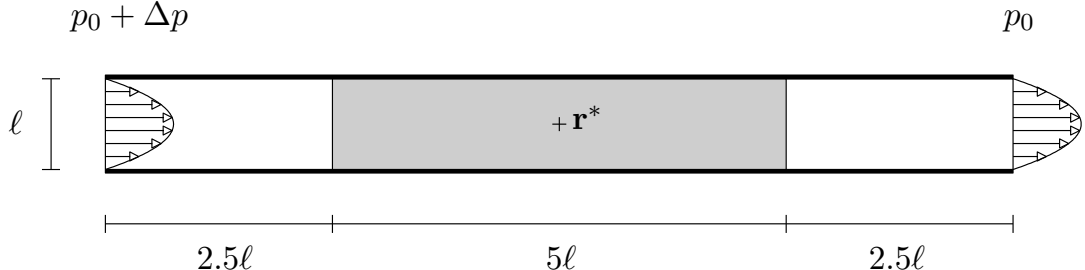


FIG. 1: Computational domain for the reverse flow example. The design domain (gray) has length 5ℓ and height ℓ , and the fluid enters and leaves the design domain through leads of length 2.5ℓ . The boundary conditions prescribe a pressure drop of Δp across the system, and the design objective is to reverse the flow direction at the point \mathbf{r}^* at center of the channel.

which can be obtained by assembling $\hat{\mathbf{L}}_4$ with $\hat{\mathbf{G}}_4 = \mathbf{0}$, $\hat{F}_4 = 1$, and $\hat{G}_4 = 0$. In the Appendix we have included a transcript of the code required to set up and solve the example from Sec. IV B below with FEMLAB. It amounts to 111 lines of code, of which the majority are spent on setting up the actual Navier–Stokes flow problem. Only a minor part goes to set up the adjoint problem and perform the sensitivity analysis. Moreover, this part contains almost no reference to the actual physical problem being solved, and therefore it should apply for any multiphysical problem that can be expressed in the divergence form Eqs. (10a)–(10c) and for any objective function of the form of Eq. (11). The code example employs, but does not include, a MATLAB implementation of the MMA optimization algorithm [9, 10].

IV. NUMERICAL EXAMPLES

In this section we present our results for topology optimization of Navier–Stokes flow for two particular model systems that we have studied. These systems have been chosen because they illustrate the dependence of the solution on the two dimensionless numbers Re and Da , measuring the importance of the inertia of the fluid and the permeability of the porous medium, respectively, relative to viscosity. Moreover we discuss the dependence of the solution on the initial condition for the material distribution.

When solving the Navier–Stokes flow problem we use the standard direct linear solver in FEMLAB in the Newton iterations. Typically we have around 6000 elements in the mesh, corresponding to 30000 degrees-of-freedom. The constrained optimization problem is solved using MMA [9], and the design iterations are stopped when the maximal change in the design field is $\|\gamma^{(k+1)} - \gamma^{(k)}\|_\infty \leq 0.01$, at which point we typically have $|\Phi^{(k+1)} - \Phi^{(k)}| < 10^{-5}$.

A. Example: a channel with reverse flow

Our first numerical example deals with the design of a structure that at a particular point inside a long straight channel can guide the flow in the opposite direction of the applied pressure drop. The corresponding problem with a prescribed flow rate was first suggested and investigated by A. Gersborg-Hansen [8]. We elaborate on it here to illustrate the importance of the choice of permeability for the porous medium.

The computational domain is shown in Fig. 1. It consists of a long straight channel of height ℓ and length $L = 10\ell$; the actual design domain, inside which the porous material is distributed, is limited to the central part of length 5ℓ . The boundary conditions prescribe a pressure drop of Δp from the inlet (left) to the outlet (right), and no-slip for the fluid on the channel side walls.

The optimization problem is stated as a minimization of the horizontal fluid velocity at the point \mathbf{r}^* at the center of the channel; i.e., the design objective is

$$\Phi = v_1(\mathbf{r}^*). \quad (32)$$

In terms of the general objective Eq. (11) this is obtained with $A \equiv v_1(\mathbf{r})\delta(\mathbf{r} - \mathbf{r}^*)$ and $B \equiv 0$. There is no explicit need for a volume constraint because neither of the extreme solutions of completely filled or empty can be optimal. When the design domain is completely filled with porous material we expect a flat flow profile with magnitude below $\Delta p/(5\ell\alpha_{\max})$. In the other extreme case when the channel is completely devoid of porous material the solution is

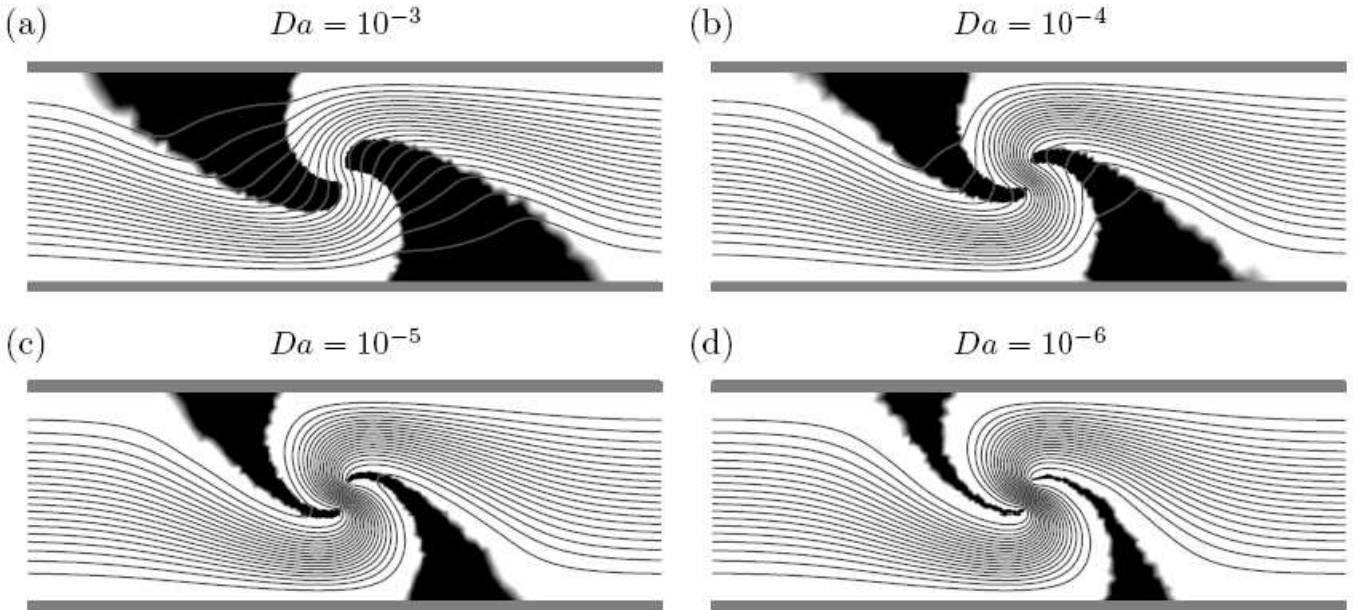


FIG. 2: Optimized structures (black) and streamlines at 5% intervals for Stokes flow ($Re = 0$) at Darcy numbers decreasing from 10^{-3} to 10^{-6} . Only the central part of length 3ℓ of the design domain is shown. The structures consist of two barriers defining an *S*-shaped channel that reverses the flow at the central point \mathbf{r}^* . As the Darcy number is decreased, the optimized structures become thinner and less permeable.

simply a parabolic Poiseuille profile with maximum

$$v_0 = \frac{\eta}{8\ell^2} \frac{\Delta p}{L}. \quad (33)$$

However, a structure that *reverses* the flow such that $v_1(\mathbf{r}^*)$ becomes negative will be superior to both these extreme cases in the sense of minimizing Φ .

1. Stokes flow limit, $Re = 0$

We first consider the Stokes flow limit of small Δp where the inertial term becomes negligible. The problem is then linear and the solution is characterized by a single dimensionless parameter, namely the Darcy number Da , Eq. (6). We have solved the topology optimization problem for different values of Da . The initial condition for the material distribution was $\gamma^{(0)} = 1$, and the parameter q determining the shape of $\alpha(\gamma)$ in Eq. (4) was set to $q = 0.1$. Anticipating that the structural details close to \mathbf{r}^* should be more important than those further away we chose a non-uniform finite element mesh with increased resolution around \mathbf{r}^* .

Fig. 2 shows the optimal structures obtained for $Da = 10^{-3}$, 10^{-4} , 10^{-5} , and 10^{-6} . They all consist of two barriers defining an *S*-shaped channel that guides the fluid in the reverse direction of the applied pressure drop. At $Da = 10^{-3}$ the two barriers are rather thick but leaky with almost all the streamlines penetrating them; as the Darcy number is decreased the optimal structures become thinner and less penetrable. This result can be interpreted as a trade-off between having either thick barriers or wide channels. Thick barriers are necessary to force the fluid into the *S*-turn, while at the same time the open channel should be as wide as possible in order to minimize the hydraulic resistance and maximize the fluid flow at the prescribed pressure drop.

Notice that if we had chosen to prescribe the flow rate through the device rather than the pressure drop, then the optimal solution would have been somewhat different. When the flow rate is prescribed, it pays to make the gap between the barriers very small and the barriers very thick in order to force the fixed amount of fluid flowing through the narrow contraction. The optimal structure is therefore one with a very large hydraulic resistance. In Ref. [8] this problem was circumvented by adding a constraint on the maximal power dissipation allowed at the given flow rate.

In order to validate the optimality of the structures computed by the topology optimization we do as follows. For each of the optimized structures from Fig. 2 we freeze the material distribution and solve the flow problem for a range Darcy numbers. The resulting family of curves for $v_1(\mathbf{r}^*)$ vs. Da is shown in Fig. 3 where it is seen that each of

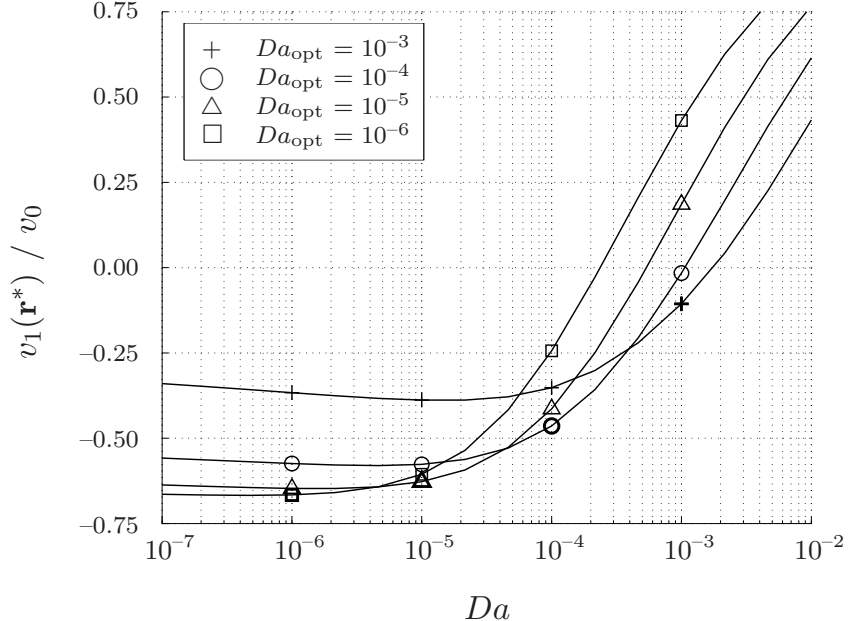


FIG. 3: Comparing the performance of the structures from Fig. 2 optimized at $Da_{\text{opt}} = 10^{-3}, 10^{-4}, 10^{-5}$, and 10^{-6} for different values of Da . The objective $v_1(\mathbf{r}^*)$ is normalized with the velocity in an empty channel, v_0 , c.f. Eq. (33).

the four structures from Fig. 2 do indeed perform better in minimizing $v_1(\mathbf{r}^*)$ than the others at the value of Da for which they are optimized.

For $Da \lesssim 10^{-5}$ the optimal value of $v_1(\mathbf{r}^*)$ tends to saturate because the thin barriers are then almost completely impermeable and the open channel cannot get much wider. Actually, in this limit the thickness of the optimized barrier structures approach the mesh resolution as seen in Fig. 2(d). When the optimal barrier thickness gets below the mesh size we have observed the appearance of artificial local optima for the barrier structure. The problem is that the thin barriers cannot continuously deform into another position without going through an intermediate structure with barriers that are thicker by at least one mesh element. Depending on the initial condition, the optimization algorithm can therefore end up with a sub-optimal structure. We have tried to work around this problem by decreasing the value of q in order to smear out the solid/void interfaces and thus reduce the cost of going through the intermediate structure. This did not work out well; the reason may be that the smearing property of a convex $\alpha(\gamma)$ was derived for the objective of minimizing the power dissipation subject to a volume constraint. In the present example we are dealing with a different objective and have no volume constraint. However, when the barrier structures are resolved with at least a few elements across them the artificial local optima tend to be insignificant. Thus the problem can be avoided by choosing a sufficiently fine mesh, or by locally refining the mesh at the solid/void interfaces based on the gradient of $\gamma(\mathbf{r})$.

Returning to Fig. 3 we notice that as Da increases all the structures perform poorly in minimizing $v_1(\mathbf{r}^*)$, as they all approach v_0 . Extrapolating this trend we might suspect that the *S*-turn topology will cease to be optimal somewhere below $Da = 10^{-3}$ simply because the porous material becomes too permable to make reversal of the flow direction possible. We have tested this hypothesis by performing an optimization at $Da = 10^{-2}$, resulting in the structure shown in Fig. 4 where the value of the objective is $v_1(\mathbf{r}^*) = 0.1v_0$. It is seen to display a different topology from those of Fig. 2, with the design domain is almost completely filled with porous material blocking the flow through the channel. Only immediately above and below the point \mathbf{r}^* we see two empty regions emerging which act to *short-circuit* the pressure and guide the flow away from \mathbf{r}^* .

Actually, in all four cases from Fig. 2, starting from an empty channel the design iterations initially converge towards a symmetric structure blocking the flow like that in Fig. 4. However at a certain point in the iterations an asymmetry in the horizontal plane is excited and the structure quickly changes to the two-barrier *S*-geometry. Whether the optimization converge to an *S*- or an inverted *S*-turn depends how the asymmetry is excited from numerical noise or irregularity in the finite element mesh; in fact the structure in Fig. 2(b) originally came out as an inverted *S* but was mirrored by hand before plotting it to facilitate comparision with the three other structures.

$$Da = 10^{-2}$$

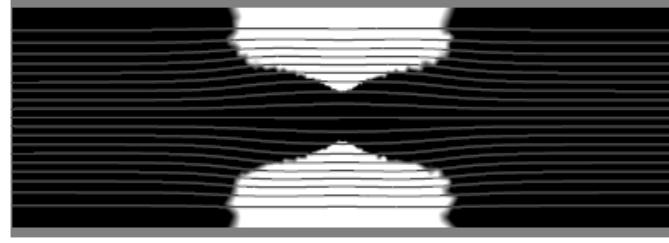


FIG. 4: Optimized structure (black) and streamlines for Stokes flow at $Da = 10^{-2}$; only the central part of length 3ℓ . The design domain is completely filled with porous material, except immediately above and below \mathbf{r}^* where two empty regions emerge. These voids divert the flow away from \mathbf{r}^* resulting in a low velocity $v_1(\mathbf{r}^*) = 0.1v_0$.

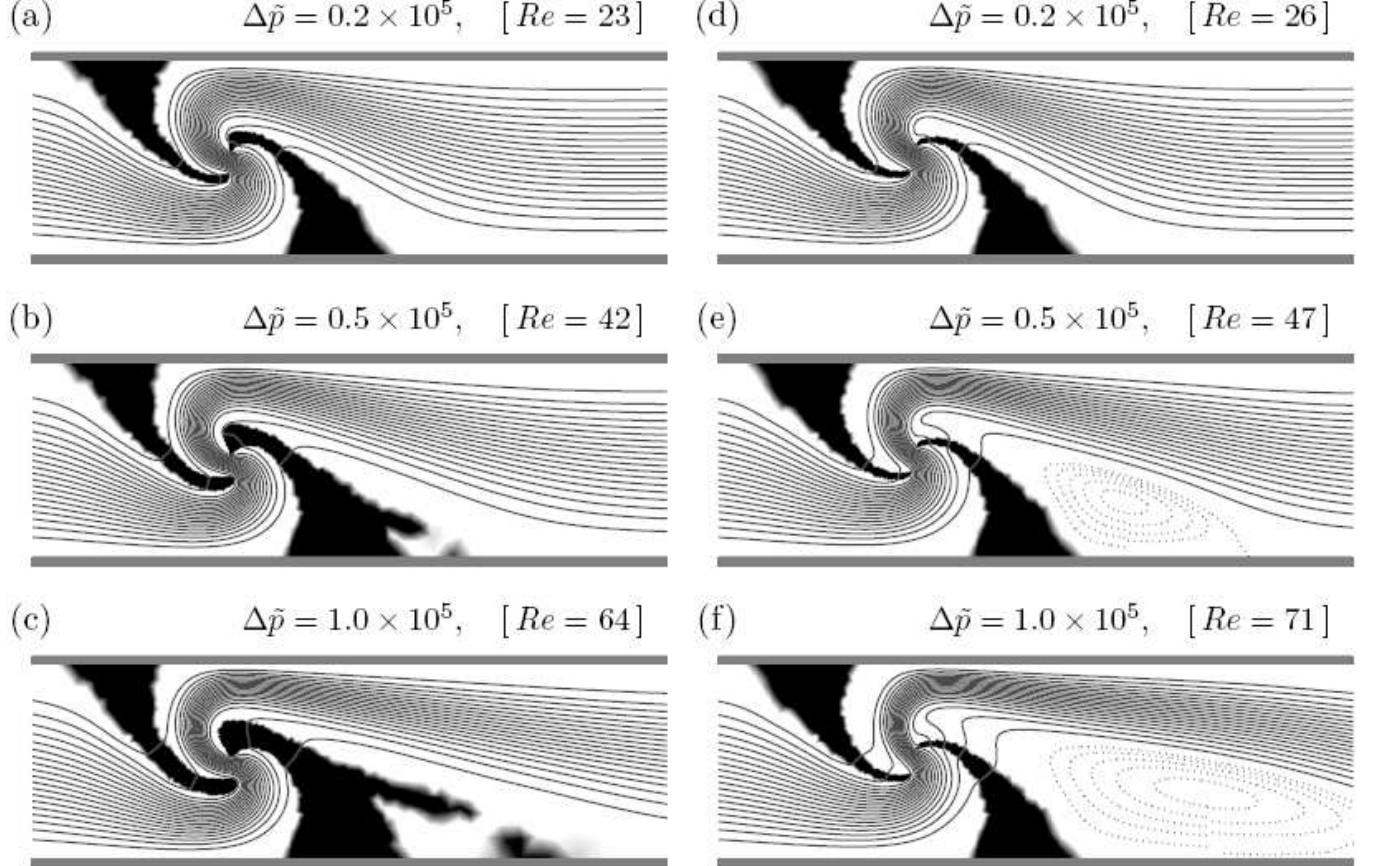


FIG. 5: Optimized structures (black) and streamlines for Navier–Stokes flow; only a part of length 3.25ℓ near the center of the channel is shown. Panel (a)-(c) to the left show the optimized structures for different values of the control parameter $\Delta\tilde{p} = \Delta p \rho \ell^2 / \eta^2$. For comparison the flow field when the corresponding structure from Fig. 2(c) is frozen and exposed to the elevated pressure drops is shown in panel (d)-(f) to the right. The Reynolds number is defined as $Re = \rho \ell v_{\max} / \eta$ where v_{\max} is the maximal velocity measured at the inlet; note that for a particular value of $\Delta\tilde{p}$, the Reynolds number is not fixed but differs slightly between left and right column.

2. Reverse flow at finite Reynolds number

We now consider flow at finite Reynolds number, characterized by the two dimensionless numbers Re and Da . The geometry and boundary conditions remain unchanged, and we fix the Darcy number at $Da = 10^{-5}$. Also, it is convenient to introduce a non-dimensional pressure drop $\Delta\tilde{p} = \Delta p \rho \ell^2 / \eta^2$.

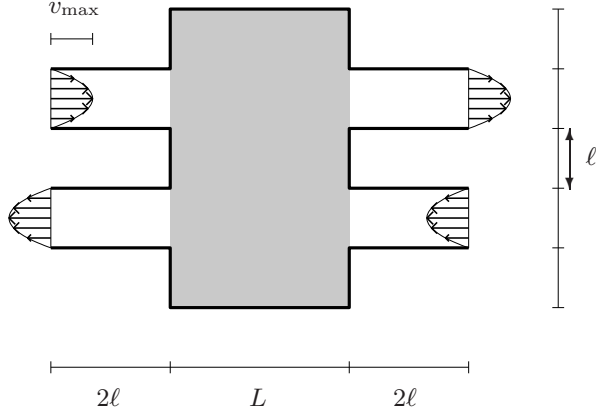


FIG. 6: Schematic illustration of the four-terminal device. Two inlet and two outlet leads (white areas) of width ℓ and length 2ℓ are attached to the design domain (gray) of width 5ℓ and length L . The flow is characterized by the Reynolds number $Re = \rho v_{\max} / \eta$, where v_{\max} is the maximal velocity at the inlets.

We have solved the topology optimization problem for different values of $\Delta\tilde{p}$, always using an empty channel as initial condition. The results are shown in Fig. 5(a)-(c) for $\Delta\tilde{p} = 0.2, 0.5$, and 1.0×10^5 , where only a few streamlines are seen to penetrate the barriers. For comparison we also consider the flow field obtained when the structure optimized for Stokes flow at $Da = 10^{-5}$ is frozen and exposed to the three different elevated pressure drops. This is shown in Fig. 5(d)-(f): as the pressure drop is increased, more and more streamlines penetrate the barriers. Moreover we find a recirculation region emerging behind the second barrier which reduces pressure drop over the neck between the barriers.

Returning to Fig. 5(a)-(c), where the structures have been optimized for the corresponding pressure drops, we find that the barriers grow thicker which reduces number of streamlines penetrating them. Also a beak-like tip grows on the second barrier that acts to bend the fluid stream down. Finally, on the back of the second barrier a wing- or spoiler-like structure appears that removes the recirculation.

In summary, our first example has demonstrated that our implementation of topology optimization works, but that the optimal design and performance may depend strongly on the choice of the Darcy number. In particular, the zero Da limit solution contains zero thickness but impermeable barriers deflecting the fluid. In order to approximate this solution at finite Da and on a finite resolution mesh it is important to choose the Darcy number small enough that even thin barriers can be almost impermeable, but large enough to avoid difficulties with artificial local optima in the discretized problem when the barrier thickness decreases below the mesh resolution. This result is important, e.g., in relation to design of fluidic diodes because these will often contain (narrow) barriers deflecting the fluid stream differently depending on the flow direction through the diode, c.f. the Tesla valve.

B. Example: a four-terminal device

Our second numerical example deals with minimization of the power dissipation in a four-terminal device subject to a volume constraint. The problem is found to exhibit a discrete change in optimal topology driven by the inertial term. The four-terminal device is related to one considered by Borrvall and Petersson for Stokes flow in Ref. [1]; the present example demonstrates the difficulty for the optimization algorithm to find the optimal topology when there are two strong candidates for the global optimum.

The computational domain, shown in Fig. 6, consists of a rectangular design domain (gray) to which two inlet and two outlet leads (white) are attached symmetrically. The boundary conditions prescribe parabolic profiles for the flow at the inlets, zero pressure and normal flow at the outlets, and no-slip on all other external boundaries. Choosing the width ℓ of the leads as our characteristic length scale, we define the Reynolds number as $Re = \rho v_{\max} / \eta$, where v_{\max} is the maximal velocity at the inlets. The Darcy number is fixed at $Da = 10^{-4}$ to obtain reasonably small leakage through the porous walls.

The optimization problem is stated as a minimization of the total power dissipation inside the computational domain, given by Eq. (7a), subject to the constraint that at most a fraction $\beta = 0.4$ of the design domain should be without porous material, c.f. Eq. (15b).

Fig. 7(a) and (b) shows the two optimal structures obtained for $Re = 20$ and 200 , respectively, in a geometry with $L = 3.5\ell$. At $Re = 20$ the optimal structure turns out to be a pair of U -turns connecting the inlets to the outlets on

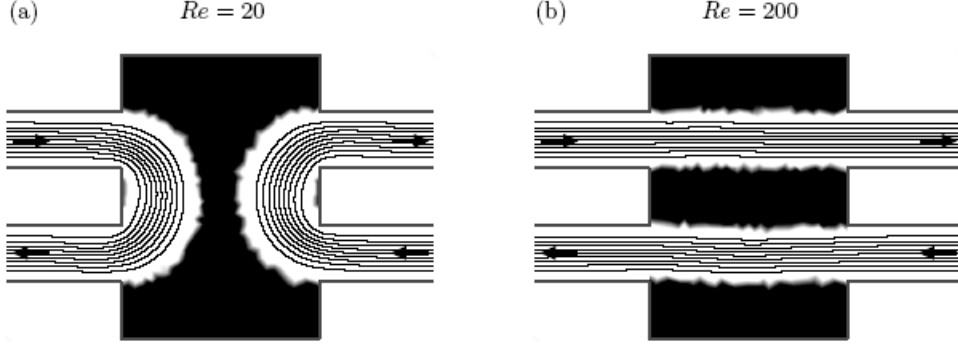


FIG. 7: Optimal structures (black) and streamlines at 10% intervals for the four-terminal device at Reynolds number $Re = 20$ and 200, respectively, in a geometry with $L = 3.5\ell$.

the same side of the design domain, while at $Re = 200$ the optimal structure is a pair of parallel channels. In order to minimize the power dissipation at low Re , the channel segments should be as short and as wide as possible, which favors the U -turns in Fig. 7(a). However, as the Reynolds number is increased, the cost of bending the fluid stream grows. When inertia dominates, larger velocity gradients appear in the long outer lane of the U -turn. This increases the dissipation compared to low Re , where more fluid flows in the short inner lane. At a certain point it will exceed the dissipation in the parallel channels solution, that can be estimated from Poiseuille flow in two straight channels, each of length $L + 4\ell$ and width ℓ ,

$$\Phi_0 = \frac{96}{9} \left(4 + \frac{L}{\ell} \right) \eta v_{\max}^2. \quad (34)$$

This is independent of inertia due to translation symmetry, and we use Φ_0 as a natural unit of power dissipation (per unit length in the third dimension) in the following.

Clearly the Reynolds number at which the transition between the two classes of solutions occurs will depend strongly on the ratio L/ℓ . For short lengths $L \lesssim 2\ell$ the parallel channels solution is expected to be optimal at all Re , whereas for long lengths $L \gtrsim 3\ell$ the U -turn solution should be significantly better than the parallel channels solution at low Re .

1. Dependence on the Reynolds number

In the following we investigate more closely the transition between the U -turns and the parallel channels solution as a function of the Reynolds number for the particular geometry $L = 3\ell$. The topology optimization problem is solved for different Re in the range 0 to 200, using a homogeneous material distribution $\gamma^{(0)} = 0.4$ as initial condition. For the parameter q determining the shape of $\alpha(\gamma)$ in Eq. (4) we use a two-step solution procedure as suggested in Ref. [1]. First the problem is solved with $q = 0.01$ in order to obtain a solution with slightly smeared-out solid/void interfaces. Next this material distribution is used as initial guess for a solution with $q = 0.1$ which generates fully discrete solid/void interfaces at the resolution of our finite element mesh.

Fig. 8(a) shows the result for the normalized power dissipation Φ/Φ_0 obtained as a function of Re . At low Reynolds numbers the optimized solutions correctly come out as U -turns with a power dissipation Φ that is clearly less than Φ_0 . However, at high Reynolds numbers $Re > 90$ the method fails because the optimized solutions continue to come out as U -turns even though this yields $\Phi/\Phi_0 > 1$. For $Re \geq 160$ the solution jumps from the simple U -turns to a hybrid with the parallel channels, as shown in the inset. The full lines in Fig. 8(a) show the result when the material distributions optimized for $Re = 0, 50$, and 180 , respectively, are frozen and the power dissipation evaluated at different Re . It is seen that the optimized solutions, marked (o), all fall on or below the full lines which confirms that they are indeed superior to the other solutions of the U -turn family. This also holds for $Re > 90$, except for the hybrid structures at $Re \geq 160$, that are actually inferior to the U -turns. Moreover, at $Re = 160$ the optimized solution falls slightly above that optimized at $Re = 180$.[17]

The difficulty is that the two families of solutions, the U -turns and the parallel channels, are both deep local minima for the power dissipation in design space. Using $\gamma^{(0)} = 0.4$ as initial condition, the initial permeability is everywhere very low, such that the porous friction almost completely dominates the inertia and viscous friction in the fluid. Therefore the iteration path in design space is biased towards low Reynolds numbers and the U -turns solution.

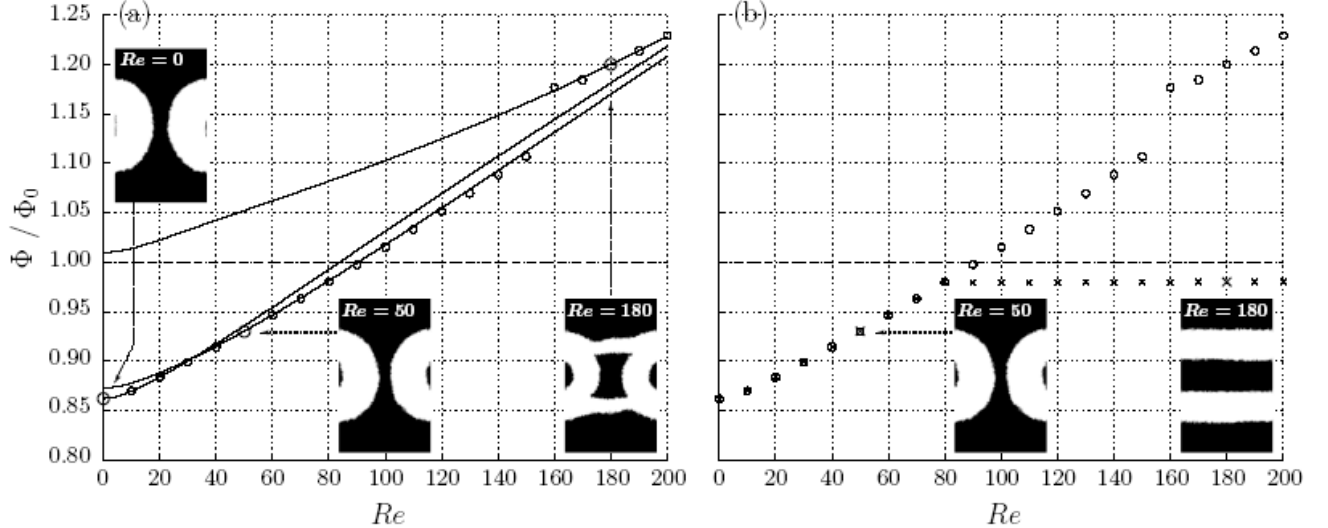


FIG. 8: Power dissipation Φ in structures optimized for different Reynolds numbers; normalized with the Poiseuille flow result Φ_0 (dashed line). (a) Markers (\circ) show results using $\gamma^{(0)} = 0.4$ as initial condition, failing to find the optimal solution for $Re > 90$. Full lines show the performance of the structures optimized at $Re = 0, 50$, and 180 , when evaluated at different Reynolds numbers. As expected, all points fall on or below the full lines, except the hybrid solutions for $Re \geq 160$. (b) Comparision between the two different initial conditions $\gamma^{(0)} = 0.4$ (\circ) and $\gamma^{(0)} = 1$ (\times), showing the success of the empty initial condition in finding the optimal solution. The crosses (\times) fall slightly below $\Phi/\Phi_0 = 1$ due to leakage through the porous walls (see the text).

In order to circumvent this problem we have tried using a completely empty design domain with $\gamma^{(0)} = 1$ as initial condition. This should remove the bias towards the U -turns and allow the optimization algorithm to take inertia into account from iteration one. The result is shown in Fig. 8(b). For $Re \leq 80$ the solutions are still U -turns, whereas for $Re \geq 90$ they come out as parallel channels. Notice that Φ/Φ_0 for the parallel channels solution is actually slightly less than unity, namely 0.98. This is due to a small amount of fluid seeping through the porous walls defining the device, which lowers the hydraulic resistance compared to the Poiseuille flow result derived for solid walls.[18]

Strictly speaking the initial condition $\gamma^{(0)} = 1$ is not a feasible solution because it the volume constraint that at most a fraction $\beta = 0.4$ of the design domain should be open channel. However, the MMA optimization algorithm penalizes this and reaches a feasible solution after a few iterations. This is controlled by choosing a penalty parameter. If the penalty for violating the constraint is small, the material is added slowly and only where it does not disturb the flow much. If the penalty is large, the material is added quickly and almost homogeneously until the constraint is satisfied. The succesful result from Fig. 8(b) was obtained with a moderate penalty. In Fig. 9 this is compared with results for smaller and larger penalty parameters, respectively. The figure shows that with the small penalization, the solution jumps to the parallel channels already at $Re = 50$ which is not optimal. For the large penalization, the solution does not jump until $Re \geq 190$. Also we observe hybrid structures similiar to those in Fig. 8(a) for $Re \geq 130$. We have thus not full control over the convergence towards the global optimum.

2. Discussion of problems with local optima

Further insight into the problem of local versus global optima is gained by inspecting the flow field in the initial material distribution $\gamma^{(0)}$. This is shown in Fig. 10 for the Stokes flow limit, $Re = 0$. The streamlines are drawn as 10% contours of the streamfunction, and Fig. 10(a) shows that for $\gamma^{(0)} = 0.4$ the streamline density is largest between the two leads on the same side of the design domain. Based on the sensitivity $\partial\Phi/\partial\gamma$ the optimization algorithm therefore decides to remove material in order to reduce the porous friction in these large-flow regions. The iteration path in design space is therefore biased towards the U -turn solution. This remains true even at finite Reynolds numbers as long as the porous friction dominates inertia.

Fig. 10(b) shows that when $\gamma^{(0)} = 1$ the streamline density is largest between the leads on the opposite side of the design domain. Because the volume constraint is violated the optimization algorithm has to place material somewhere, which it does in the low-flow regions. The solution is therefore biased towards the parallel channels. Indeed if the

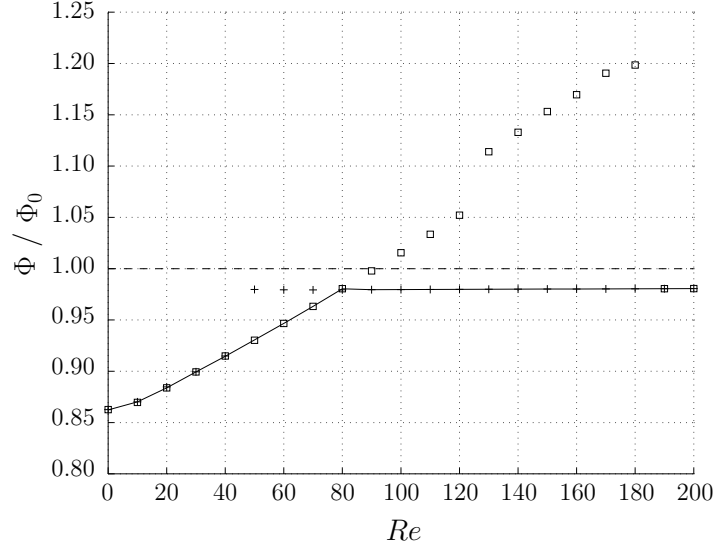


FIG. 9: Comparision between structures optimized with the initially non-feasible material distribution $\gamma^{(0)} = 1$ for different penalty parameters in optimization algorithm, revealing the difficulty in choosing the condition for finding the global optimum. Full line: the successful result from Fig. 8(b) with moderate penalty; (+): lower penalty yielding wrong result for $40 < Re < 80$; (□) higher penalty yielding wrong results for $80 < Re < 190$.

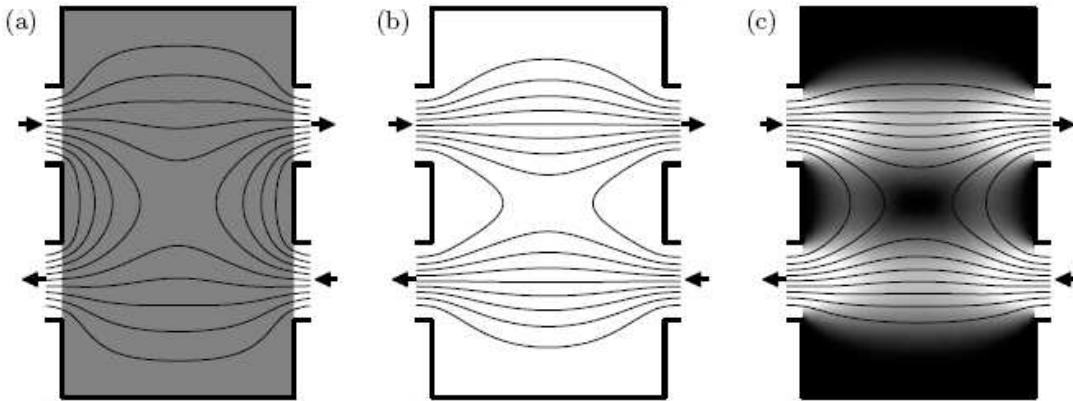


FIG. 10: Flow distributions at $Re = 0$, $L = 3\ell$ and $q = 0.01$. (a) Initial design field $\gamma^{(0)} = 0.4$. (b) Initial design field $\gamma^{(0)} = 0.4$. (c) The optimal design field $\gamma^{(*)}$ obtained at $Da = 10^{-2}$.

penalty is chosen very small, the solution comes out as parallel channels even for Stokes flow at $L = 3\ell$, which is far from optimal. When the penalty is larger and the material is added faster, we move away from this adiabatic solution and closer to the situation for $\gamma^{(0)} = 0.4$.

The additional complexity associated with making a proper choice of the penalty parameter is somewhat inconvenient. We have therefore attempted to construct a more convex problem by increasing the initial permeability. This can be done either by increasing the Darcy number, or by decreasing the parameter q , c.f. Eq. (4). Fig. 10(c) shows the optimal solution $\gamma^{(*)}$ obtained for $Da = 10^{-2}$ and $q = 0.01$ at $Re = 0$. At this level the problem is convex because the solution is independent of the initial condition. Using this material distribution as initial guess and gradually decreasing the permeability to $Da = 10^{-4}$ and $q = 0.1$ we correctly end up in the U -turn solution. However, it is evident from Fig. 10(c) that $\gamma^{(*)}$ has a fair amount of parallel channels nature. Using this solution procedure of gradually decreasing the permeability at higher Reynolds numbers therefore result in a transition to the parallel channels solution already for $Re \geq 30$, which is clearly not optimal. Moreover, when the Reynolds number is increased and the inertia starts to play in, the system tends to loose convexity even at the high permeability.

In summary, the topology optimization has difficulties in finding the global optimum for the problem. There are two strong candidates for the optimal structure, and the solution found is sensitive to the initial condition for the material distribution. Using an empty channel as initial condition, the method is able to find the correct solution for

all Reynolds numbers. However, this successful result depends on a proper choice of the penalty parameter in the MMA algorithm. By using a high initial permeability of the porous medium, it is possible to convexify the problem at low Reynolds numbers. Continuation of this solution to the desired low permeability does not generally lead to the global minimum of the non-convex problem, though.

In the original paper Ref. [1] it was argued that in Stokes flow the true optimal design should be rather insensitive to the choice of the Darcy number, although the dissipated power may deviate quite a lot from the zero Da limit. In our work we have observed that the actual solution found by the topology optimization may depend a great deal on the choice of the Darcy number, whereas the dissipated power should approach the zero Da limit roughly as \sqrt{Da} .

V. CONCLUSION

Based on the work of Borrvall and Petersson [1] we have extended the topology optimization of fluid networks to cover the full incompressible Navier–Stokes equations in steady-state. Our implementation of the method is based of the commercial finite element package FEMLAB, which reduces the programming effort required to a minimum. Formulating the objective function in the general form Eq. (11) and performing the sensitivity analysis with the governing equations on the generic divergence form Eqs. (10a)–(10c) makes the implementation very compact and transparent. Moreover the code for this analysis should remain almost the same for any problem expressed in this way, whereas the code for describing the physical problem of course changes. Topology optimization of multiphysics problems can therefore be performed almost as easy as solving the PDE of a single realization of the underlying physical problem. Also defining the optimization objective is easy since it simply amounts to stating the expression for A and B in Eq. (11).

Our implementation of topology optimization has been tested on two fluidics examples, both illustrating the influence of different quantities and conditions on the efficiency of the optimization method.

The first example, a channel with reversed flow, illustrates the influence of the Reynolds number Re and the Darcy number Da on the solutions. We have shown that the choice of Da has a strong impact on the solution when the structure contains barriers to deflect the fluid stream.

The second example, minimization of the power dissipation in a four-terminal device, show the problems of determining the global minimum when two strong minima are competing. This problem is highly non-convex, and we have shown that the solution depends on the initial condition. For a homogeneous material distribution, $\gamma^{(0)} = 0.4$, the porous friction dominates and the solution is not the global optimum in all cases. Using an empty channel as the initial state, $\gamma^{(0)} = 1$, inertia plays a role from the beginning, and more correct solutions are obtained. However, the initial condition in fact violates the volume constraint, and the part of the optimization routine correcting this depends on a penalty factor. Unfortunately, the chosen value for this factor influences the solution, and in some cases the solution is not the global minimum. Increasing the Darcy number makes the problem more convex, but continuation from large to small Da , i.e., from high to low permeability of the material, does not generally end up in global optimum.

In conclusion, we have shown that our implementation of topology optimization is a useful tool for designing fluidic devices.

VI. ACKNOWLEDGEMENT

We are grateful to Ole Sigmund and Allan Gersborg-Hansen for illuminating discussions on the topology optimization method, and to Krister Svanberg for providing us with the MATLAB code for the MMA routine. This work is partly supported by The Danish Technical Research Council, Grant No. 26-03-0037.

- [1] T. Borrvall T, J. Petersson, *Int. J. Numer. Meth.* **41**, 77 (2003)
- [2] M. P. Bendsøe, N. Kikuchi, *Comp. Meth. Appl. Mech. Eng.* **2**, 197 (1988)
- [3] *Topology Optimization: Theory, Methods and Applications* by M. P. Bendsøe and O. Sigmund, Springer Verlag (Berlin, 2003).
- [4] H. A. Eschenauer, N. Olhoff, *Appl. Mech. Rev.* **54**, 331 (2001)
- [5] J. S. Jensen, *J. Sound and Vibration* **266**, 1053 (2003)
- [6] J. S. Jensen, O. Sigmund, *Appl. Phys. Letters* **84**, 2022 (2004)
- [7] O. Sigmund, A. Gersborg-Hansen, and R. B. Haber, proc. Nordic Matlab Conference 2003, L. Gregersen (Ed.), Comsol A/S, Søborg, Denmark, pp. 237-242.
- [8] *Topology optimization of incompressible Newtonian flows at moderate Reynolds numbers* by A. Gersborg-Hansen, M.Sc.-thesis, Technical University of Denmark (2003)

- [9] K. Svanberg, SIAM J. Optim. **12**, 555 (2002).
- [10] A MATLAB implementation of the MMA optimization algorithm [9] can be obtained (free of charge for academic purposes) from Krister Svanberg, KTH, Sweden. Email: krille@math.kth.se.
- [11] *Course of Theoretical Physics, Vol. 6, Fluid Mechanics* by L. D. Landau and E. M. Lifshitz, Butterworth and Heinemann, 2nd edition, (Oxford, 2000)
- [12] P. Michaleris, D. A. Tortorelli, C. A. Vidal, Int. J. Numer. Methods Eng. **37**, 2471 (1994)
- [13] FEMLAB reference manual. Stockholm: COMSOL AB
- [14] Borrvall and Petersson suggest a model for plane flow between two parallel surfaces of varying separation $h(\mathbf{r})$. The power dissipation due to out-of-plane shears is modelled by an absorption term $-\alpha \mathbf{v}$, where $\mathbf{v}(\mathbf{r})$ is the average velocity between the surfaces and $\alpha(\mathbf{r}) = 12\eta/h(\mathbf{r})^2$. In their model it is therefore natural to operate with a non-zero $\alpha_{\min} = 12\eta/h_{\max}^2$ in Eq. (4).
- [15] In particular this is the case when the inlets and outlets are chosen as straight channels sufficiently long that prescribing a parabolic Poiseuille profile can be justified, see Figs. 1 and 6.
- [16] Another common choice is the discontinuous and piecewise constant element for the design variable. Notice that for second and higher order Lagrange elements the condition $0 \leq \gamma_n \leq 1$ does not imply $0 \leq \gamma(\mathbf{r}) \leq 1$ for all \mathbf{r} because of under- or overshoot at sharp zero-one transitions in γ . This in turns can result in negative α , c.f. Eq. (4), which is unphysical and destroys the convergence of the algorithm.
- [17] This could be an indication that the hybrid structures are not local optima in design space after all, but rather a very narrow saddle point that the optimization algorithm has a hard time getting away from.
- [18] The flow in a straight channel of width ℓ bounded by two porous walls of thickness ℓ can easily be found analytically. At $Da = 10^{-4}$ the hydraulic resistance of this system is 94% of that for a channel of width ℓ bounded by solid walls, and it approaches this zero Da limit only as \sqrt{Da} . When $L = 3\ell$ we therefore expect a power dissipation $\Phi/\Phi_0 = (3 \times 0.94 + 4)/7 = 0.97$ for the parallel channels solution, including the leads. This is close to the observed 0.98.

APPENDIX A: FEMLAB IMPLEMENTATION

```

% FEMLAB CODE FOR THE 4-TERMINAL DEVICE OF SEC. 4.2
clear fem femadj
% DEFINE REYNOLDS NUMBER, Darcy NUMBER, LENGTH OF DESIGN DOMAIN, AND VOLUME FRACTION
Re = 50;
Da = 1e-4;
L0 = 3.0;
beta = 0.4;
% DEFINE GEOMETRY, MESH, AND SUBDOMAIN/BOUNDARY GROUPS [SEE FIG. 6]
fem.geom = rect2(0,L0,0,5) + rect2(-2,0,1,2) + rect2(-2,0,3,4) + rect2(L0,L0+2,1,2) ...
+ rect2(L0,L0+2,3,4);
fem.mesh = meshinit(fem,'Hmaxsub',[3 0.125]);
% subdomain groups 1:design domain 2:inlet/outlet leads
fem.equ.ind = {[3] [1 2 4 5]};
% boundary groups 1:walls 2:inlets 3:outlets 4:interior
fem.bnd.ind = {[2:3 5:8 10 12:14 16:18 20:22] [4 23] [1 24] [9 11 15 19]};
% DEFINE SPACE COORDINATES, DEPENDENT VARIABLES, AND SHAPE FUNCTIONS
fem.sdim = {'x' 'y'};
fem.dim = {'u' 'v' 'p' 'gamma'};
fem.shape = [2 2 1 1];
% DEFINE CONSTANTS
fem.const.rho = 1;
fem.const.eta = 1;
fem.const.umax = Re;
fem.const.alphamin = 0;
fem.const.alphamax = 1/Da;
fem.const.q = 0.1;
Phi0 = 96*fem.const.eta*(L0+4)*fem.const.umax^2/9;
% DEFINE EXPRESSIONS ON SUBDOMAIN AND BOUNDARY GROUPS
fem.equ.expr = {'A' 'eta*(2*ux*ux+2*vy*vy+(uy+vx)*(uy+vx))+alpha*(u*u+v*v)', ...
'alpha' {'alphamax+(alphamin-alphamax)*gamma*(1+q)/(q+gamma)', '0'}};
fem.bnd.expr = {'B' '0'};

% DEFINE GOVERNING EQUATIONS AND INITIAL CONDITIONS [SEE EQS. (8) AND (9)]
fem.form = 'general';
fem.equ.shape = {[1:4] [1:3]}; % only define gamma on subdomain group 1
fem.equ.ga = {{{'-p+2*eta*ux'} 'eta*(uy+vx)'} {'eta*(uy+vx)' '-p+2*eta*vy'} {0 0} {0 0}};
fem.equ.f = {'rho*(u*ux+v*uy)+alpha*u' 'rho*(u*vx+v*vy)+alpha*v' 'ux+vy' 1};
fem.equ.init = {[0 0 0 beta]};
% DEFINE BOUNDARY CONDITIONS
fem.bnd.shape = {[1:3]}; % do not define gamma on any boundaries
fem.bnd.r = {'u' 'v' 0 0} ... % walls: no-slip

```

```

{'u*nx+4*umax*s*(1-s)', 'v' 0 0} ... % inlets: parabolic profile
{0 'v' 0 0} ... % outlets: normal flow
{0 0 0 0}; % interior: nothing
fem.bnd.g = {[0 0 0 0]}; % zero prescribed external forces everywhere
% PERFORM LINEARIZATION, DEGREE-OF-FREEDOM ASSIGNMENT, AND ASSEMBLE INITIAL CONDITION
fem = femdiff(fem);
fem.xmesh = meshextend(fem);
fem.sol = asseminit(fem);

% DEFINE STRUCTURE FOR COMPUTING RIGHT-HAND-SIDE IN ADJOINT PROBLEM [SEE EQ. (29)]
femadj = fem;
femadj.equ.ga = {{{'diff(A,ux)', 'diff(A,uy)'}, {'diff(A,vx)', 'diff(A,vy)'}} ... % inlets: parabolic profile
{'diff(A,px)', 'diff(A,py)'}, {'diff(A,gammamax)', 'diff(A,gammamin)'}}};
femadj.equ.f = {{'diff(A,u)', 'diff(A,v)', 'diff(A,p)', 'diff(A,gamma)'}};
femadj.bnd.g = {{'diff(B,u)', 'diff(B,v)', 'diff(B,p)', 'diff(B,gamma)'}};
femadj.xmesh = meshextend(femadj);
% GET INDICES OF DESIGN VARIABLE IN THE GLOBAL SOLUTION VECTOR (fem.sol.u)
i4 = find(asseminit(fem,'Init',{'gamma' 1}, 'Out', 'U')));
% COMPUTE VOLUME BELOW DESIGN VARIABLE BASIS FUNCTIONS
L = assemble(fem,'Out',{'L'});
Vgamma = L(i4);
Vdomain = sum(Vgamma);
% GET INDICES OF VELOCITY-PRESSURE VARIABLES
i123 = find(asseminit(fem,'Init',{'u' 1 'v' 1 'p' 1}, 'Out', 'U')));

% DEFINE VARIABLES PARAMETERS FOR MMA OPTIMIZATION ALGORITHM [SEE REF. [9,10]]
a0 = 1;
a = 0;
c = 20;
d = 0;
xmin = 0;
xmax = 1;
xold = fem.sol.u(i4);
xolder = xold;
low = 0;
upp = 1;

% DESIGN LOOP FOR THE ACTUAL TOPOLOGY OPTIMIZATION
for iter = 1:100
    % SOLVE NAVIER-STOKES FLOW PROBLEM TO UPDATE VELOCITY AND PRESSURE
    fem.sol = femlin(fem,'Solcomp',{'u' 'v' 'p'}, 'U', fem.sol.u);
    % SOLVE ADJOINT PROBLEM FOR LAGRANGE MULTIPLIERS
    [K N] = assemble(fem,'Out',{'K' 'N'}, 'U', fem.sol.u);
    [L M] = assemble(femadj,'Out',{'L' 'M'}, 'U', fem.sol.u);
    femadj.sol = femlin('In',{'K' K(i123,i123)}, 'L' L(i123) 'M' zeros(size(M)) 'N' N(:,i123));
    % SENSITIVITY ANALYSIS
    gamma = fem.sol.u(i4);
    Phi = postint(fem,'A','Edim',2) + postint(fem,'B','Edim',1);
    dPhigamma = L(i4) - K(i123,i4)*femadj.sol.u;
    % PERFORM MMA STEP TO UPDATE DESIGN FIELD
    x = gamma;
    f = Phi/Phi0; % gamma'*Vgamma/Vdomain - beta;
    dfdx = dPhigamma/Phi0; dgdx = Vgamma'/Vdomain;
    d2fdx2 = zeros(size(gamma)); d2gdx2 = zeros(size(gamma));
    [xnew,y,z,lambda,ksi,eta,mu,zeta,s,low,upp] = mmasub(1,length(gamma),iter, ...
    x,xmin,xmax,xold,xolder,f,dfdx,d2fdx2,g,dgdx,d2gdx2,low,upp,a0,a,c,d);
    xolder = xold; xold = x; gamma = xnew;
    % TEST CONVERGENCE
    if iter >= 100 | max(abs(gamma-xold)) < 0.01
        break
    end
    % UPDATE DESIGN VARIABLE
    u0 = fem.sol.u; u0(i4) = gamma;
    fem.sol = femsol(u0);
    % DISPLAY RESULTS FOR EACH ITERATION STEP
    disp(sprintf('Iter.:%3d Obj.: %8.4f Vol.: %6.3f Change: %6.3f', ...
    iter,f,xold'*Vgamma,max(abs(xnew-xold))));
    postplot(fem,'arrowdata',{'u' 'v'},'tridata','gamma','trimap','gray')
    axis equal; shg; pause(0.1)
end

```